

Energy–time entanglement from a monolithically integrated quantum dot on silicon

Marcel Hohn,^{1, a)} Imad Limame*,^{1, a)} Peter Ludewig,^{2, 3} Chirag C. Palekar,¹ Aris Koulas-Simos,¹ Kerstin Volz,^{2, 3} and Stephan Reitzenstein¹

¹⁾*Institute for Physics and Astronomy, Technical University of Berlin, Hardenbergstraße 36, D-10623 Berlin, Germany^{a)}*

²⁾*mar.quest | Marburg Center for Quantum Materials and Sustainable Technologies, Philipps University Marburg, 35032 Marburg, Germany*

³⁾*Department of Physics, Philipps University Marburg, Hans Meerwein Str. 6, 35032 Marburg, Germany*

(*Electronic mail: imad.limame@tu-berlin.de)

(Dated: 1 July 2026)

Scalable quantum photonic technologies require deterministic sources of entangled photons that are compatible with established semiconductor manufacturing platforms. While self-assembled III–V semiconductor quantum dots are among the most promising sources of on-demand entanglement generation, their integration with silicon-based architectures remains a central challenge. Here, we demonstrate energy–time entanglement from a single InGaAs/GaAs quantum dot monolithically grown on a silicon substrate. Under coherent two-photon excitation, we achieve coherent control of the biexciton–exciton cascade, evidenced by Rabi oscillations and dressed-state formation. Using a four-channel Franson interferometer, we observe phase-dependent two-photon interference with visibilities up to $(64.0 \pm 7.0)\%$ for an 80 ps integration window (and $(49.4 \pm 1.9)\%$ for a 1600 ps window), approaching the threshold for Bell inequality violation at short time scales. These results establish monolithically integrated III–V-on-silicon quantum dots as promising sources of energy–time entangled photons for scalable quantum photonic technologies.

I. INTRODUCTION

Semiconductor III–V quantum dots (QDs) have emerged as a leading solid-state platform for quantum photonic technologies based on the generation of indistinguishable and entangled single photons^{1–4}. Over the past decade, QDs have demonstrated near-ideal quantum optical performance, including high single-photon purity⁵, high entanglement fidelity^{6,7}, and high photon indistinguishability⁸, while simultaneously achieving high extraction efficiencies when integrated into photonic nanostructures^{9,10}. Importantly, their emission wavelength can be engineered from the near-infrared to the telecom C-band^{11,12}, making them highly versatile for both fiber-based and on-chip quantum networks.

These exceptional optical properties have positioned QDs as key quantum light sources for a range of quantum information protocols, including quantum key distribution (QKD)^{13,14}, boson sampling^{15,16}, and entanglement swapping^{17,18}. In parallel, substantial progress has been made toward scalable device architectures through deterministic QD positioning techniques. Approaches such as site-controlled growth using buried stressors^{19,20}, nanohole-template-assisted nucleation²¹, inverted pyramids²², and post-growth deterministic integration via in-situ or marker-based lithography^{23–25} have enabled precise spatial control of emitters, even facilitating the realization of integrated quantum photonic circuits²⁶. Furthermore, the monolithic integration of III–V photonic devices—including lasers, detectors, and, as demonstrated here, quantum emitters—on silicon represents a major milestone toward the seamless integration of silicon photonics

with III–V nanophotonic platforms for both classical and quantum technologies^{27,28}. In the context of InGaAs/GaAs QDs, the introduction of a GaP intermediate buffer layer on silicon substrate has enabled the epitaxial growth of high-quality single-photon-emitting QDs operating both in the near-infrared around 930 nm and in the telecom O-band^{27,29}.

A central feature of semiconductor QDs is their ability to generate entangled photon pairs via the biexciton–exciton (XX–X) radiative cascade³⁰. To date, most investigations of entangled-photon generation in QDs have focused on polarization entanglement^{7,31–33}. However, the achievable entanglement fidelity is fundamentally limited by the fine-structure splitting (FSS) of the exciton state, which originates from structural asymmetries and inhomogeneous strain distributions introduced during the growth process. Although significant progress has been made toward reducing the FSS through approaches such as droplet-etched GaAs/AlGaAs QDs³⁴ and the growth of InGaAs QDs on (111)-oriented GaAs substrates^{35,36}, these strategies often involve trade-offs, including restricted emission wavelength tunability or reduced optical quality.

Energy-time entanglement provides an attractive alternative that is intrinsically insensitive to FSS. In this approach, entanglement is encoded in the temporal and spectral correlations of photon pairs rather than in their polarization degree of freedom, thereby circumventing symmetry-related limitations^{37,38}. While energy-time entanglement has been extensively studied using spontaneous parametric down-conversion (SPDC) sources⁴, the probabilistic nature of SPDC fundamentally limits source brightness, scalability, and, in some quantum communication protocols, security. Semiconductor QDs, by contrast, offer a deterministic route to the generation of entangled photon pairs. Energy–time entan-

^{a)}These authors contributed equally to this work.

gement from QDs has been experimentally demonstrated using time-bin and Franson-type interferometric measurements, including full quantum state tomography^{39,40}. Furthermore, the generation of multi-photon time-bin-entangled states has been reported⁴¹, highlighting the potential of QDs as scalable sources for advanced quantum photonic protocols.

Here, we report on the generation of energy-time entangled photon pairs under coherent excitation from InGaAs QDs integrated monolithically on silicon substrate. Energy–time interference measurements under two-photon excitation (TPE) yield Franson visibilities of up to $(64 \pm 7)\%$ for an 80 ps integration window, demonstrating non-classical energy–time correlations while remaining below the threshold required for a Bell-inequality violation⁴². The remaining limitations in visibility are attributed to residual non-interfering contributions rather than to fundamental constraints of the platform, highlighting silicon-integrated QDs as a promising route toward scalable, silicon-compatible quantum photonic technologies.

II. MONOLITHIC INTEGRATION ON SILICON

The investigated QD-heterostructure was grown by metal-organic chemical vapor deposition (MOCVD) in a two-step epitaxial process, schematically illustrated in Fig. 1 and described in detail in Ref.²⁷. In the first step, an exactly oriented 300 mm Si (001) substrate was overgrown in an AIXTRON Crius R CCS twin-reactor system with a 5 μm Si:P buffer layer, followed by the deposition of a GaP III–V nucleation layer⁴⁴. This nucleation layer serves as a critical interface between the non-polar Si substrate and the polar III–V material system, thereby suppressing the formation of anti-phase domains⁴⁵. Subsequently, a sequence of AlGaAs/GaAs and GaInP dislocation-filtering layers was deposited, acting both as lattice-accommodating layers and as an effective means to reduce the threading dislocation density (TDD). These layers facilitate dislocation bending and annihilation, significantly improving the crystalline quality of the III/V heterostructure^{44,45}. The first epitaxial stage was completed by the growth of a 2.5 μm GaAs layer, which provides a high-quality virtual GaAs substrate suitable for subsequent QD epitaxy (Fig. 1, bottom). Following this initial growth, the wafer was cleaved into $4 \times 4 \text{ cm}^2$ samples and transferred to an AIX 200/4 MOCVD reactor for the second epitaxial step. The second epitaxial stage starts with the deposition of a 300 nm GaAs buffer layer at 700 °C under a high V/III ratio of 200, ensuring excellent crystalline quality. Subsequently, 32.5 periods of $\text{Al}_{0.90}\text{Ga}_{0.10}\text{As}/\text{GaAs}$ are grown at the same temperature, forming a highly reflective bottom distributed Bragg reflector (DBR) designed to enhance photon out-coupling into the 0.69 NA collection optics of the μPL setup. The individual layer thicknesses correspond to $\lambda/4$, with 68 nm for GaAs and 81 nm for $\text{Al}_{0.90}\text{Ga}_{0.10}\text{As}$. The structure is completed by a λ/n GaAs cavity (274 nm) incorporating a 0.40 nm $\text{In}_{0.33}\text{Ga}_{0.67}\text{As}$ seed layer at its center. A growth interruption of 40 s is applied to promote the self-assembly of QDs, yielding an areal density on the order of

$1 \times 10^9 \text{ cm}^{-2}$. We refer to Ref.²⁷ for details on the structural quality and surface morphology of the grown sample.

III. COHERENT BIEXCITON EXCITATION AND VERIFICATION OF THE BIEXCITON-EXCITON CASCADE

Following epitaxial growth, the sample is mounted on a three-axis piezoelectric stage inside a closed-cycle helium cryostat and cooled to 4 K. Optical excitation is provided by a tunable continuous-wave (CW) laser and the QD emission is collected in a confocal configuration using a 0.69 NA aspheric lens. The emission spectra are recorded with a silicon CCD coupled to a monochromator equipped with a 1500 lines/mm grating. Time-resolved photoluminescence (TRPL) and second-order autocorrelation measurements, $g^{(2)}(\tau)$, are performed by detecting spectrally filtered QD emission with superconducting nanowire single-photon detectors (SNSPDs) providing a temporal resolution of 30 ps. More details on the used μPL setup are provided in Ref.²⁷.

Using power- and polarization-resolved μPL measurements we identified the exciton (X) and biexciton (XX) transitions, and the investigated QD is excited via TPE, as shown in Fig. 2. Panels (a) and (b) present representative μPL spectra acquired at excitation powers of $0.048 \times P_{\text{sat}}$ and $0.25 \times P_{\text{sat}}$, respectively. At low excitation power, the X and XX emission lines are observed at approximately 1.3045 eV (950.43 nm) and 1.3068 eV (948.76 nm). The excitation laser is tuned to 1.3055 eV, such that two laser photons resonantly drive the two-photon transition from the ground state to the biexciton state via a virtual intermediate state. As the excitation power is increased, the resulting XX–X cascade emission becomes increasingly pronounced. Since the excitation wavelength lies outside the suppression range of the available notch filters, the residual laser light is rejected by cross-polarized detection and spatial mode filtering through the single-mode collection fiber. At elevated excitation powers, the emergence of dressed-state splitting (Fig. 2(b)) provides clear evidence of coherent driving of the QD^{46,47}. In particular, the splitting into the $L_{+,0}$ and $R_{+,0}$ states is resolved in the cross-polarized detection configuration. The observed dressed-state splitting provides direct evidence of coherent light–matter interaction and enables extraction of the Rabi frequency, which scales linearly with the square root of the excitation power.

The cross-correlation of the XX–X cascade was investigated at an excitation power of $0.17 \times P_{\text{sat}}$, and the resulting histogram of coincidence counts is shown in Fig. 2(c). The histogram exhibits pronounced antibunching at negative delay times, corresponding to the arrival of single biexciton (XX) photons, followed by strong bunching at positive delays associated with the subsequent exciton (X) emission. This asymmetric correlation signature unambiguously confirms the cascaded nature of the XX–X radiative decay process. The inset reveals an additional long-time bunching behavior, which is typical for semiconductor QDs and attributed to blinking dynamics and re-excitation processes within the QD system⁴⁸.

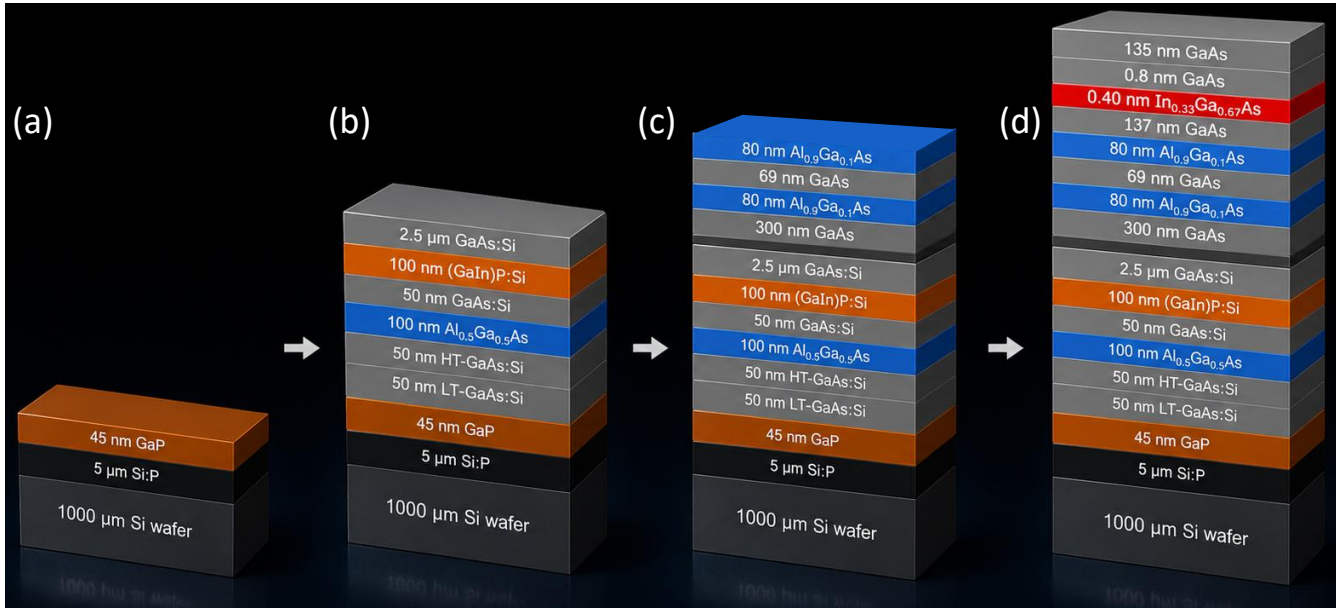


FIG. 1. Schematic of the epitaxial layer structure grown on a (001)-oriented Si substrate. The lower stack comprises a Si-compatible GaP nucleation layer (a), followed by GaAs-, AlGaAs-, and GaInP-based layers for strain accommodation and dislocation reduction (b), culminating in a high-quality virtual GaAs substrate. The upper structure consists of a GaAs buffer, a backside DBR (32.5 pairs of GaAs/Al_{0.90}Ga_{0.10}As) (c), and an active region formed by self-assembled In_{0.33}Ga_{0.67}As QDs embedded within a λ/n GaAs cavity (d).⁴³

IV. INTRINSIC TEMPORAL AND COHERENCE CONSTRAINTS OF THE BIEXCITON-EXCITON CASCADE

In this section, we assess the coherence properties and temporal dynamics of the XX–X cascade relevant for energy–time entanglement experiments, TRPL measurements were performed under off-resonant pulsed excitation at 1.3931 eV (890 nm) using a tunable optical parametric oscillator (OPO) delivering 2 ps pulses at a repetition rate of 80 MHz. The extracted decay times are (574 ± 45) ps for the X transition and (286 ± 12) ps for the XX transition, consistent with the expected radiative lifetime relation between the two states, $T_{1,X} \approx 2T_{1,XX}$. Both lifetimes are substantially shorter than the radiative decay times of approximately 1–1.5 ns typically reported for comparable InGaAs/GaAs QDs grown on GaAs substrates and on silicon without Purcell enhancement²⁷. This comparatively short radiative lifetimes observed in the present sample are likely a consequence of the relatively low nominal indium concentration (33%), which promotes enhanced electron–hole wavefunction overlap and, consequently, an increased oscillator strength, in agreement with previous reports⁴⁹. Franson interference requires an interferometer delay for which the indistinguishable short-short (SS) and long-long (LL) two-photon amplitudes overlap within the selected coincidence window, while the short-long (SL) and long-short (LS) contributions remain temporally distinguishable. In addition, the two-photon coherence must be preserved over the interferometer imbalance. The intrinsic time ordering and lifetime hierarchy of the XX–X cascade therefore impose an important constraint: for a given interferometer delay, the temporal overlap between the SS and LL amplitudes decreases

as the biphoton wavepacket becomes short compared to the path imbalance. Consequently, the achievable Franson visibility is highly sensitive to the combined influence of radiative lifetimes, coherence times, temporal postselection window, and interferometer delay. While energy–time entanglement is generally less sensitive to FSS than polarization entanglement, residual exciton splitting can still indirectly affect phase stability in interferometric measurements under finite temporal resolution. Nevertheless, the cascade ordering remains the dominant intrinsic limitation, as it fundamentally restricts the temporal overlap between the SS and LL pathways and thereby sets an upper bound on the achievable Franson interference visibility, which become particularly sensitive to the coherence properties of the cascade.

Additionally, the single-photon coherence properties of the X and XX transitions were investigated using Michelson interferometry under TPE at an excitation power of $0.17 \times P_{\text{sat}}$. The extracted coherence times are $T_{2,XX} = (128 \pm 4)$ ps and $T_{2,X} = (91 \pm 3)$ ps, respectively. For both transitions, $T_2 < 2T_1$ indicating the presence of pure dephasing in addition to radiative decay. Interestingly, the longer coherence time observed for the XX transition suggests a higher degree of phase preservation, consistent with its direct coherent excitation via TPE, whereas the X state is populated indirectly through spontaneous radiative decay in the cascade. It is further noted that the measured coherence times exhibit a pronounced dependence on excitation power, as reduced excitation conditions mitigate laser-induced decoherence mechanisms such as charge noise activation, local heating, and re-excitation processes.

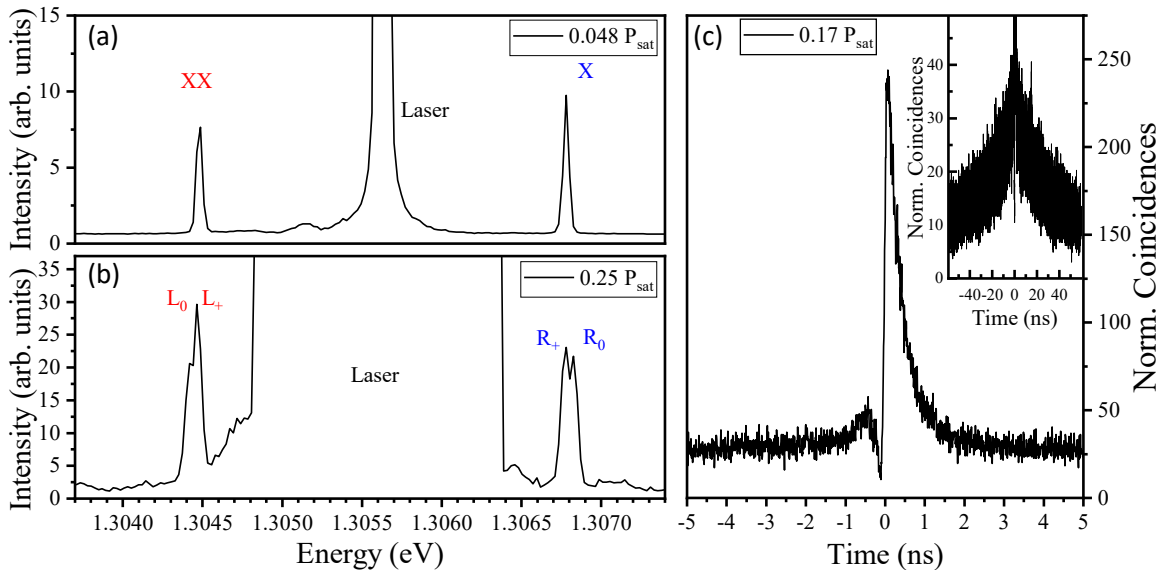


FIG. 2. Emission spectra of the investigated QD under CW resonant TPE at excitation powers of $0.048 P_{\text{sat}}$ (a) and $0.25 P_{\text{sat}}$ (b). At elevated power (b), the emergence of dressed-state splitting evidences coherent driving of the transition. Laser suppression is achieved via polarization filtering in a cross-polarized configuration. (c) Cross-correlation histogram between biexciton (XX) and exciton (X) emission at $0.17 P_{\text{sat}}$. The pronounced antibunching at negative delays and bunching at positive delays unambiguously confirm the cascaded emission process. The observed Rabi oscillations further substantiate coherent excitation. Inset: long-timescale bunching attributed to blinking and re-excitation dynamics.

V. FRANSON INTERFEROMETRY

In this section, we first describe the implemented Franson interferometer setup (Fig. 3), followed by the corresponding measurements performed on the QD under study.

The experiment is based on two unbalanced Michelson interferometers, mounted on a vibration-isolated optical table and enclosed in a housing that suppresses stray light and air fluctuations. Although the interferometric setup operates in free space, all input and output ports are fiber-coupled to enable a modular configuration compatible with a transmission spectrometer, which provides spectral separation of the XX (red) and X (blue) emission, as well as fiber-based single-photon detection, as displayed in Fig. 3. Each interferometer arm consists of a non-polarizing 50/50 beamsplitter and two retroreflectors. The use of retroreflectors instead of planar mirrors ensures self-aligned beam retracing, thereby significantly simplifying alignment and improving long-term phase stability. The interferometers are configured with a short (S) and a long (L) arm, defining an optical path-length difference of $\Delta L = 43$ cm, corresponding to a temporal delay of $\Delta T = 1.4$ ns (with typical arm lengths of $L = 25$ cm and $S = 3.5$ cm). The short-arm mirrors and one long-arm mirror are mounted on translation stages for coarse path-length matching, while both short-arm mirrors are additionally equipped with piezoelectric actuators, enabling nanometer-scale phase control. The XX and X emission channels, spectrally filtered by the transmission spectrometer, are coupled into the interferometers via single-mode fibers. After recombination at the beamsplitter, emission at both output ports of each interfer-

ometer is collected using fiber couplers and routed to a four-channel SNSPD system. Detection events are time-tagged using a time-correlated single-photon counting (TCSPC) module, providing a combined temporal resolution of approximately 100 ps and a system detection efficiency of approximately 85%. In an initial configuration, only one output port per interferometer (CH1, CH2) was monitored, resulting in a 50% reduction in usable signal. The setup was subsequently upgraded with additional fiber couplers and routing optics, enabling full four-channel detection (CH1–CH4) and improved coincidence efficiency.

For energy–time entanglement characterization, coincidence correlations between the interferometer outputs are recorded, yielding the four relevant pairwise combinations CH1[^]CH3, CH1[^]CH4, CH2[^]CH3, and CH2[^]CH4. Second-order interference is obtained by scanning the total interferometer phase via piezoelectric modulation of the short-arm lengths. The coincidence counts are recorded as a function of phase using an automated data acquisition system.

Due to the low signal level associated with single-photon emission measurements, long-term interferometric stability is required. To achieve this, we employ active feedback stabilization using a reference laser integrated into the same setup, enabling phase stability over several hours with a precision on the order of tens of nanometers. Phase-stabilization is implemented by using a reference laser (CW diode laser) featuring a coherence length of several kilometers which is fiber-coupled and split into both Michelson interferometers via a fiber beamsplitter. The interference visibility of the stabilization signal depends sensitively on the laser polarization, since

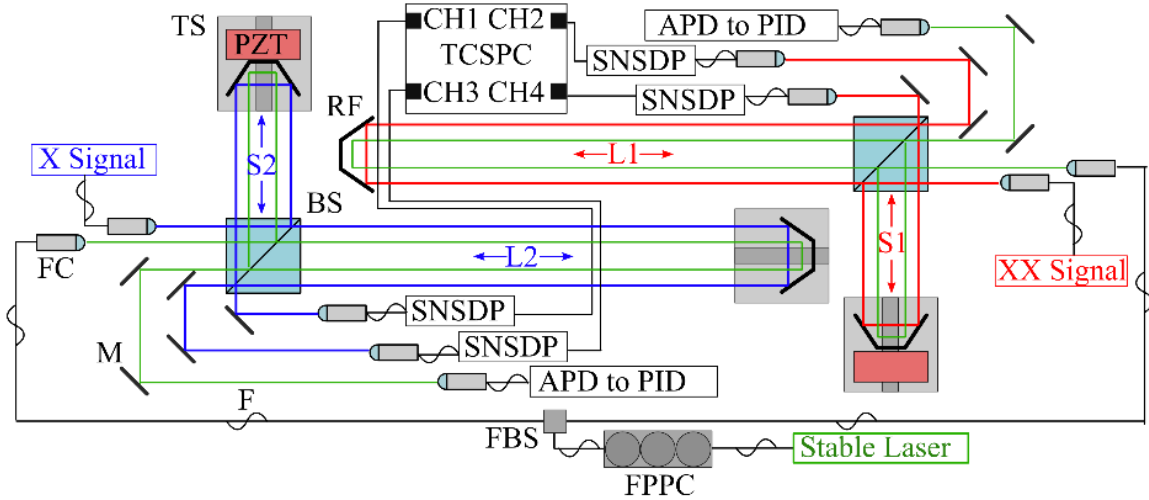


FIG. 3. Four-channel Franson interferometer configuration: XX and X photons are spectrally separated by a transmission spectrometer and fiber-coupled into two unbalanced Michelson interferometers (red and blue arms). Each interferometer comprises a non-polarizing 50/50 beamsplitter and a pair of retroreflectors, with the short-arm mirrors mounted on piezoelectric actuators enabling precise phase control. A co-propagating reference laser (green) is employed for active phase stabilization of both interferometers.

orthogonally polarized components do not interfere. Therefore, a fiber polarization controller (fiber paddle) was inserted into the reference-laser fiber path to optimize the polarization state. The laser is then out-coupled along a parallel path (green in Fig. 3) relative to the signal path, and the first-order interference signal was detected by two silicon single-photon avalanche diodes (SPADs; Excelitas single-photon counting modules) and recorded with a time tagger, which provide the feedback signal for a PID controller. Each interferometer operates with an independent PID loop controlling the piezo actuator in the short arm.

VI. ENERGY-TIME ENTANGLEMENT OF THE BIEXCITON-EXCITON CASCADE

In the following section, we investigate the degree of energy-time entanglement of the X-XX cascade emitted from the QD under study by means of Franson interferometry. To suppress excitation-induced dephasing (EID) and re-excitation processes, both of which are known to significantly limit Franson interference visibility^{38,50}, the measurements were performed at a low excitation power of $0.023 P_{\text{sat}}$. Following a complete phase scan across one full interference period, the coincidence histograms recorded at the maximum and minimum interference conditions are presented in Fig. 4(a-d), using a temporal bin width of 80 ps. The post-selection windows are indicated by the blue-shaded regions, with a width of 1600 ps applied to both the central and SPs. At the observed low coincidence rates, the red line denotes the non-interfering background contribution. Importantly, the interfering LL/SS events are well separated from the adjacent SL and LS peaks, enabling unambiguous temporal post-selection of the entangled photon pairs. Note, the data were

post-selected in two steps. First, coincidence events corresponding to entangled photon pairs were selected within a temporal window of 0–1600 ps (blue-shaded regions). Second, the non-interfering background contribution was subtracted, as indicated by the red line.

To extract the interference visibility, the coincidence counts within the central peak (central blue-shaded region) were integrated for each relative phase setting over the interval from -690 nm to 300 nm and subsequently normalized to the corresponding side-peak coincidences (side blue-shaded regions in Fig. 4(a-d)). The results of this analysis are presented in Figure 4(e) and (f) for an integration window of 1600 ps. The solid colored curves represent sinusoidal fits used to determine the visibility for the respective channel combinations. A pronounced variation in the extracted visibilities is observed between different detector-channel combinations, ranging from a maximum of $(49.4 \pm 1.9)\%$ for $\text{CH2}^{\wedge}\text{CH4}$ to a minimum of $(44.6 \pm 2.2)\%$ for $\text{CH1}^{\wedge}\text{CH4}$. Under ideal interferometric conditions, such deviations are not expected and therefore indicate residual path imbalances, most likely originating from non-ideal beamsplitter ratios within the interferometer arms. In this context, the highest measured visibility of $(49.4 \pm 1.9)\%$ obtained for $\text{CH2}^{\wedge}\text{CH4}$ constitutes the least imbalance affected estimate of the intrinsic two-photon interference visibility, since path imbalances can only reduce the experimentally observed visibility during a full phase scan and cannot artificially enhance it.

Nevertheless, for consistency, we report the average visibility obtained from the two detector-channel combinations using an integration window of 1600 ps. The resulting Franson interference visibility as a function of the chosen temporal integration window is presented in Fig. 4(g). We observe a continuous reduction in the extracted interference visibility from $(64 \pm 7)\%$ for an 80 ps integration window to $(47 \pm 2)\%$

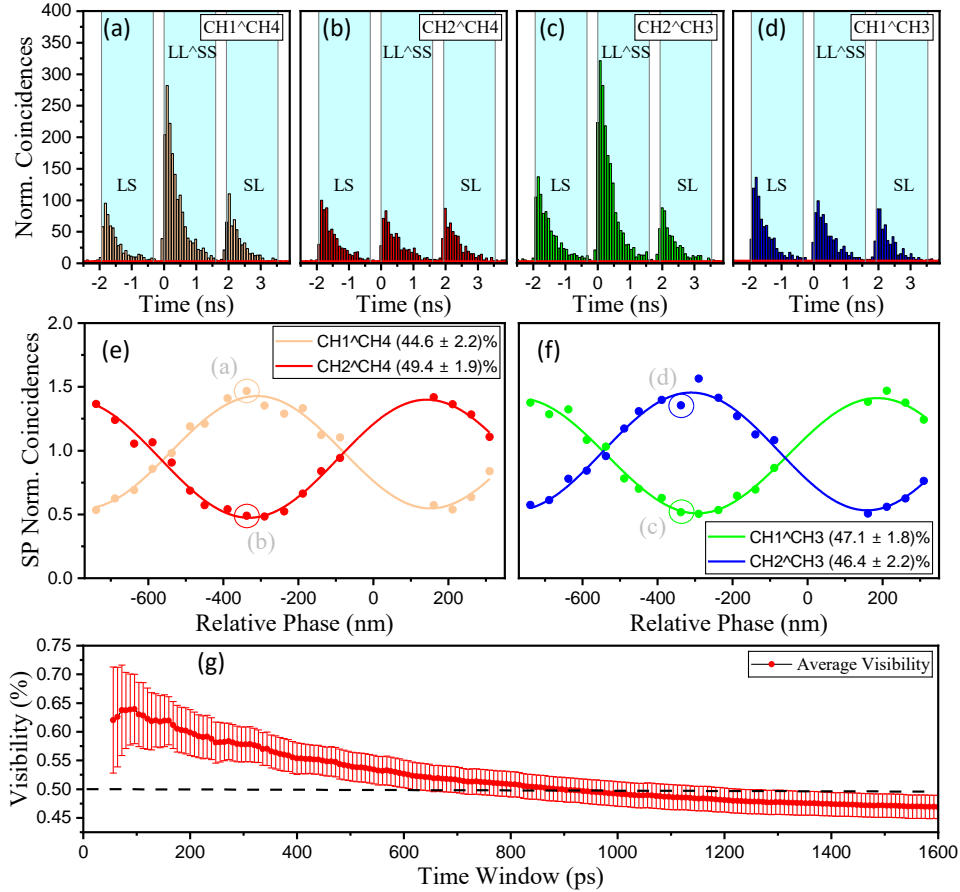


FIG. 4. Franson interference measurements of the investigated QD grown on silicon, performed under two-photon resonant excitation at $P = 0.023 P_{\text{sat}}$. (a–d) Coincidence histograms recorded at interference maxima and minima of the LL/SS path contributions, shown with a temporal binning of 80 ps. The cyan-shaded region denotes the 1600 ps integration window used to extract the interference signal, while the red line indicates the non-interfering background contribution. (e,f) Phase-dependent LL/SS coincidence counts, normalized to the side peaks (SPs), exhibiting high-contrast sinusoidal oscillations (solid lines: fits), with extracted visibilities indicated in the legend. (g) Mean two-photon interference visibility as a function of integration window width. The dashed line indicates the 50% level, which is the threshold for identifying non-classical light emission.

for a 1600 ps window. Previous studies have attributed such behavior to an increasing contribution of background events at larger temporal integration windows^{4,38}. In these reports, background subtraction was shown to render the extracted visibility largely independent of the selected window width. In contrast, the data presented in Figure 4 already include background subtraction, yet the reduction in visibility persists. This observation therefore indicates the presence of a residual non-interfering contribution within the selected coincidence peak.

Several mechanisms may account for this behavior. First, systematic uncertainties in the determination of the background level from fits to the long-time bunching contribution become increasingly significant for larger integration windows. While the correlated coincidence signal decays with increasing delay time, any residual offset remains effectively constant and therefore contributes more strongly to the integrated counts at wider windows. Notably, the long-time bunching observed in monolithically integrated InGaAs/GaAs

QDs on silicon is more accurately described by a Gaussian-like contribution, in contrast to the exponential behavior commonly reported for InGaAs/GaAs QDs grown on native GaAs substrates⁴⁸. This deviation suggests the presence of more intricate background dynamics that are difficult to fully disentangle from the interferometric cascade signal. Consequently, a small residual background component may remain after subtraction and progressively reduce the extracted visibility as the integration window is increased.

A further aspect relevant to the Franson interference experiment is the relation between the interferometer delay and the radiative lifetimes of the emitter. The path imbalance has to be sufficiently large to temporally separate the non-interfering SL and LS contributions from the central SS–LL peak and to suppress residual single-photon interference. At the same time, the interfering two-photon amplitudes must retain phase coherence over this delay. The radiative lifetimes of the XX and X transitions determine the temporal extent of the cascade wavepacket and therefore set the natural time scale on

which the interferometer delay has to be chosen. For the present emitter, with decay times of (286 ± 12) ps for XX and (574 ± 45) ps for X, a delay on the order of several nanoseconds imposes a stringent coherence requirement and may reduce the effective overlap of the interfering SS and LL contributions. A shorter path imbalance could therefore be beneficial, provided that the central and SPs remain clearly distinguishable. However, this cannot be verified from the present data alone and should be regarded as an optimization route for future experiments rather than as a conclusive explanation of the reduced visibility.

The measured Franson interference visibility of up to $(64 \pm 7)\%$ for an 80 ps integration window demonstrates a competitive degree of two-photon coherence in monolithically integrated InGaAs/GaAs QDs on silicon. In comparison to state-of-the-art III/V QD sources, which typically report Franson or time-bin visibilities in the range of $\approx 71\%$ ³⁸ to 84% ⁴⁰, depending on excitation scheme, spectral filtering, and interferometric stability, our results place the present platform within the established performance window for non-classical energy–time entangled photon generation, despite the additional complexity introduced by heterogeneous integration on silicon. Importantly, while record-high visibilities in optimized InAs/GaAs systems grown on native substrates often rely on highly engineered photonic structures and ultra-low background conditions, the present device operates under monolithic integration constraints that are inherently more demanding, yet still preserves a clear non-classical interference signature. The observed reduction in visibility with increasing integration window, down to $(47 \pm 2)\%$ at 1600 ps, further distinguishes the present system from idealized literature benchmarks, where background-subtracted visibilities are typically largely invariant with respect to the post-selection window size. This deviation highlights that, in integrated III/V-on-Si platforms, residual non-interfering contributions and interferometer imperfections are more pronounced than in bulk or hybrid fiber-based implementations.

From the perspective of quantum information technology, these results are particularly significant. Energy–time entangled photon pairs generated in a silicon-compatible material system provide a direct pathway toward on-chip quantum communication architectures that are inherently resilient to the FSS of the quantum emitter. Moreover, the monolithic integration of the emitter on silicon enables deterministic coupling to photonic circuits, offering a route toward large-scale quantum photonic networks, multiplexed entangled photon sources, and integrated quantum repeater nodes. In particular, the demonstrated coherence of the XX–X cascade under TPE supports its applicability for heralded entanglement distribution protocols and time-bin encoded quantum key distribution schemes.

Looking ahead, several concrete optimization pathways can be implemented. In particular, improved interferometric balance, reduced residual background emission, and tailoring of the interferometer delay to more closely match the radiative lifetimes of the XX and X states are expected to significantly enhance the achievable visibility and may enable violation of a Bell inequality in future device iterations. Com-

bined with ongoing advances in the epitaxial quality of QDs grown on silicon, these improvements position epitaxial InGaAs/GaAs QDs on silicon as a promising candidate for scalable quantum photonic hardware, bridging the gap between high-performance quantum emitters and industrial silicon technology.

CONCLUSIONS

Overall, the results obtained highlight the strong potential of epitaxially grown InGaAs/GaAs QDs on silicon as a scalable platform for the generation of energy–time entangled photon pairs and the realization of coherent quantum photonic technologies. By combining monolithic QD integration with coherent excitation of the XX–X cascade, the present platform enables the generation of non-classical light states that are intrinsically robust against FSS and therefore circumvent a major limitation of polarization-entangled photon sources. The observation of Franson interference visibilities of up to $(64 \pm 7)\%$, from epitaxially grown InGaAs/GaAs QDs on silicon demonstrates the preservation of two-photon coherence throughout the biexciton–exciton radiative cascade and confirms the ability of this platform to generate non-classical photonic states under coherent excitation.

Although the observed visibility remains below the threshold for Bell inequality violation due to residual non-interfering contributions, our analysis indicates that these limitations arise predominantly from technical and experimental factors rather than from fundamental constraints of the developed III/V-on-silicon material platform. Further optimization of the interferometric architecture, background suppression, and matching of the interferometer delay to the emitter dynamics is therefore expected to yield significant improvements in the attainable degree of entanglement. Taken together, our findings establish monolithically integrated InGaAs/GaAs QDs on silicon as a promising and CMOS-compatible route toward scalable quantum photonic circuits capable of generating coherent and entangled photonic states for applications in quantum communication, quantum networking, and distributed quantum information processing.

AUTHOR CONTRIBUTIONS

M. H. designed and built the four-channel Franson interferometer, performed the μ PL experiments, and carried out the data analysis and led evaluation of the results. I. L. epitaxially grew the upper part of the sample, including the QDs and DBR mirror. P. L. performed the growth and optimization of the initial GaP/Si template. C. C. P. and A. K.-S. contributed to the interpretation of the results and supported the preparation of the manuscript. K. V., S. R., and I. L. conceived and supervised the project. The manuscript was written by K. V., S. R., and I. L. with contributions from all authors.

CONFLICTS OF INTEREST

The authors have no conflicts to disclose.

DATA AVAILABILITY

The data that support the findings of this study are available from the corresponding author upon reasonable request.

ACKNOWLEDGEMENTS

The research leading to these results received funding from the Federal Ministry of Research, Technology and Space (BMFTR) through projects 16KISQ014 and 16KISQ087K, from the German Research Foundation (DFG) through projects RE2974/23-1 and INST 131/795-1 FUGG, and from the Berlin Senate through Berlin Quantum (BQ). The authors also thank Kathrin Schatke, Praphat Sonka, Heike Oppermann, and Stefan Bock for their technical support. Furthermore, the authors acknowledge Martin von Helversen and Daniel Vajner for their invaluable support and stimulating scientific discussions.

- ¹P. Senellart, G. Solomon, and A. White, *Nature Nanotechnology* **12**, 1026–1039 (2017).
- ²T. Heindel, J.-H. Kim, N. Gregersen, A. Rastelli, and S. Reitzenstein, *Advances in Optics and Photonics* **15**, 613 (2023).
- ³M. Esmann, S. C. Wein, and C. Antón-Solanas, *Advanced Functional Materials* **34**, 2315936 (2024).
- ⁴G. B. Xavier, J.-Å. Larsson, P. Villoresi, G. Vallone, and A. Cabello, *npj Quantum Information* **11**, 01072 (2025).
- ⁵L. Schweickert, K. D. Jöns, K. D. Zeuner, S. F. Covre da Silva, H. Huang, T. Lettner, M. Reindl, J. Zichi, R. Trotta, A. Rastelli, and V. Zwiller, *Applied Physics Letters* **112**, 093106 (2018).
- ⁶T. Huber, L. Ostermann, M. Prilmüller, G. S. Solomon, H. Ritsch, G. Weihs, and A. Predojević, *Phys. Rev. B* **93**, 201301(R) (2016).
- ⁷C. Chen, J.-Y. Yan, H.-G. Babin, J. Wang, X. Xu, X. Lin, Q. Yu, W. Fang, R.-Z. Liu, Y.-H. Huo, H. Cai, W. E. I. Sha, J. Zhang, C. Heyn, A. D. Wieck, A. Ludwig, D.-W. Wang, C.-Y. Jin, and F. Liu, *Nature Communications* **15**, 5792 (2024).
- ⁸S. Reitzenstein, in *Comprehensive Semiconductor Science and Technology*, Comprehensive Semiconductor Science and Technology, Vol. 2, edited by R. Fornari, M. Grundmann, V. Darakchieva, and P. Fay (Elsevier, Amsterdam, 2024).
- ⁹X. Ding, Y. He, Z.-C. Duan, N. Gregersen, M.-C. Chen, S. Unsleber, S. Maier, C. Schneider, M. Kamp, S. Höfling, C.-Y. Lu, and J.-W. Pan, *Physical Review Letters* **116**, 020401 (2016).
- ¹⁰J. Yang, Z. Rao, C. Song, M. Rao, Z. Zheng, L. Liu, X. Peng, Y. Yu, and S. Yu, *Photonics Research* **12**, 2130 (2024).
- ¹¹M. Sartison, L. Engel, S. Kolatschek, F. Olbrich, C. Nawrath, S. Hepp, M. Jetter, P. Michler, and S. L. Portalupi, *Applied Physics Letters* **113**, 032103 (2018).
- ¹²N. Hauser, M. Bayerbach, J. Kaupp, Y. Reum, G. Peniakov, J. Michl, M. Kamp, T. Huber-Loyola, A. T. Pfenning, S. Höfling, and S. Barz, *Nature Communications* **17**, 537 (2026).
- ¹³E. Waks, K. Inoue, C. Santori, D. Fattal, J. Vuckovic, G. S. Solomon, and Y. Yamamoto, *Nature* **420**, 762–762 (2002).
- ¹⁴T. Heindel, C. A. Kessler, M. Rau, C. Schneider, M. Fürst, F. Hargart, W.-M. Schulz, M. Eichfelder, R. Roßbach, S. Nauerth, M. Lermer, H. Weier, M. Jetter, M. Kamp, S. Reitzenstein, S. Höfling, P. Michler, H. Weinfurter, and A. Forchel, *New Journal of Physics* **14**, 083001 (2012).
- ¹⁵J. Loredano, M. Broome, P. Hilaire, O. Gazzano, I. Sagnes, A. Lemaitre, M. Almeida, P. Senellart, and A. White, *Physical Review Letters* **118**, 130503 (2017).
- ¹⁶H. Wang, W. Li, X. Jiang, Y.-M. He, Y.-H. Li, X. Ding, M.-C. Chen, J. Qin, C.-Z. Peng, C. Schneider, M. Kamp, W.-J. Zhang, H. Li, L.-X. You, Z. Wang, J. Dowling, S. Höfling, C.-Y. Lu, and J.-W. Pan, *Physical Review Letters* **120**, 230502 (2018).
- ¹⁷F. Basso Basset, M. B. Rota, C. Schimpf, D. Tedeschi, K. D. Zeuner, S. F. Covre da Silva, M. Reindl, V. Zwiller, K. D. Jöns, A. Rastelli, and R. Trotta, *Physical Review Letters* **123**, 160501 (2019).
- ¹⁸M. Zopf, R. Keil, Y. Chen, J. Yang, D. Chen, F. Ding, and O. G. Schmidt, *Physical Review Letters* **123**, 160502 (2019).
- ¹⁹A. Strittmatter, A. Holzbecher, A. Schliwa, J. Schulze, D. Quandt, T. D. Germann, A. Dreismann, O. Hitzemann, E. Stock, I. A. Ostapenko, S. Rodt, W. Unrau, U. W. Pohl, A. Hoffmann, D. Bimberg, and V. Haisler, *physica status solidi (a)* **209**, 2411–2420 (2012).
- ²⁰K. Gaur, A. Barua, S. Tripathi, L. J. Roche, S. Wilksen, A. Steinhoff, S. Baraz, N. Nitin, C. C. Palekar, A. Koulas-Simos, I. Limame, P. Mudi, S. Rodt, C. Gies, and S. Reitzenstein, *Light: Science & Applications* **15**, 02343 (2026).
- ²¹C. Schneider, A. Huggenberger, M. Gschrey, P. Gold, S. Rodt, A. Forchel, S. Reitzenstein, S. Höfling, and M. Kamp, *physica status solidi (a)* **209**, 2379–2386 (2012).
- ²²E. Pelucchi, S. Watanabe, K. Leifer, B. Dwir, and E. Kapon, *Physica E: Low-dimensional Systems and Nanostructures* **23**, 476 (2004), proceedings of the Fifth International Workshop on Epitaxial Semiconductors on Patterned Substrates and Novel Index Surfaces (ESPS-NIS).
- ²³A. Dousse, L. Lanco, J. Suffczyński, E. Semenova, A. Miard, A. Lemaitre, I. Sagnes, C. Roblin, J. Bloch, and P. Senellart, *Physical Review Letters* **101**, 267404 (2008).
- ²⁴M. Gschrey, F. Gericke, A. Schüssler, R. Schmidt, J.-H. Schulze, T. Heindel, S. Rodt, A. Strittmatter, and S. Reitzenstein, *Applied Physics Letters* **102**, 251113 (2013).
- ²⁵Y.-M. He, J. Liu, S. Maier, M. Emmerling, S. Gerhardt, M. Davanço, K. Srinivasan, C. Schneider, and S. Höfling, *Optica* **4**, 802 (2017).
- ²⁶S. Li, Y. Yang, J. Schall, M. von Helversen, C. Palekar, H. Liu, L. Roche, S. Rodt, H. Ni, Y. Zhang, Z. Niu, and S. Reitzenstein, *ACS Photonics* **10**, 2846–2853 (2023).
- ²⁷I. Limame, P. Ludewig, C.-W. Shih, M. Hohn, C. C. Palekar, W. Stolz, and S. Reitzenstein, *Optica Quantum* **2**, 117 (2024).
- ²⁸R. Koszica, A. M. Skipper, B. Shi, G. Leake, M. Zylstra, J. Herman, Y. Liu, C. Zhang, D. Harame, J. Klamkin, and J. Bowers, *ACS Photonics* **12**, 5173–5178 (2025).
- ²⁹S. Tripathi, K. Gaur, P. Mudi, P. Ludewig, A. Kosarev, K. Volz, I. Limame, and S. Reitzenstein, “Stark-tunable o-band single-photon sources based on deterministically fabricated quantum dot–circular bragg gratings on silicon,” (2026).
- ³⁰O. Benson, C. Santori, M. Pelton, and Y. Yamamoto, *Physical Review Letters* **84**, 2513–2516 (2000).
- ³¹N. Akopian, N. H. Lindner, E. Poem, Y. Berlatzky, J. Avron, D. Gershoni, B. D. Gerardot, and P. M. Petroff, *Physical Review Letters* **96**, 130501 (2006).
- ³²R. J. Young, R. M. Stevenson, P. Atkinson, K. Cooper, D. A. Ritchie, and A. J. Shields, *New Journal of Physics* **8**, 29 (2006).
- ³³D. Huber, M. Reindl, Y. Huo, H. Huang, J. S. Wildmann, O. G. Schmidt, A. Rastelli, and R. Trotta, *Nature Communications* **8**, 15506 (2017).
- ³⁴Y. H. Huo, A. Rastelli, and O. G. Schmidt, *Applied Physics Letters* **102**, 152105 (2013).
- ³⁵C. D. Yerino, P. J. Simmonds, B. Liang, D. Jung, C. Schneider, S. Unsleber, M. Vo, D. L. Huffaker, S. Höfling, M. Kamp, and M. L. Lee, *Applied Physics Letters* **105**, 251901 (2014).
- ³⁶M. von Helversen, A. V. Haisler, M. P. Daurtsev, D. V. Dmitriev, A. I. Toropov, S. Rodt, V. A. Haisler, I. A. Derebezov, and S. Reitzenstein, *physica status solidi (RRL) – Rapid Research Letters* **16**, 2200133 (2022), <https://onlinelibrary.wiley.com/doi/pdf/10.1002/pssr.202200133>.
- ³⁷Y.-N. Sun, Y. Zou, G. Chen, J.-S. Tang, H.-Q. Ni, M.-F. Li, G.-W. Zha, Z.-C. Niu, Y.-J. Han, C.-F. Li, and G.-C. Guo, *Optics Express* **25**, 1778 (2017).
- ³⁸M. Hohn, K. Barkemeyer, M. von Helversen, L. Bremer, M. Gschrey, J.-H. Schulze, A. Strittmatter, A. Carmele, S. Rodt, S. Bounouar, and S. Reitzen-

- stein, *Physical Review Research* **5**, L022060 (2023).
- ³⁹H. Jayakumar, A. Predojević, T. Kauten, T. Huber, G. S. Solomon, and G. Weihs, *Nature Communications* **5**, 4251 (2014).
- ⁴⁰L. Ginés, C. Pepe, J. Gonzales, N. Gregersen, S. Höfling, C. Schneider, and A. Predojević, *Optics Express* **29**, 4174 (2021).
- ⁴¹J. P. Lee, B. Villa, A. J. Bennett, R. M. Stevenson, D. J. P. Ellis, I. Farrer, D. A. Ritchie, and A. J. Shields, *Quantum Science and Technology* **4**, 025011 (2019).
- ⁴²J. S. Bell, *Physics Physique Fizika* **1**, 195–200 (1964).
- ⁴³OpenAI, “ChatGPT (GPT-5.5),” <https://chatgpt.com> (2026), large language model, accessed July 2026.
- ⁴⁴K. Volz, A. Beyer, W. Witte, J. Ohlmann, I. Németh, B. Kunert, and W. Stolz, *Journal of Crystal Growth* **315**, 37–47 (2011).
- ⁴⁵A. Beyer, B. Haas, K. I. Gries, K. Werner, M. Luysberg, W. Stolz, and K. Volz, *Applied Physics Letters* **103**, 032107 (2013).
- ⁴⁶G. Jundt, L. Robledo, A. Högele, S. Fält, and A. Imamoglu, *Physical Review Letters* **100**, 177401 (2008).
- ⁴⁷C. Sánchez Muñoz, F. P. Laussy, C. Tejedor, and E. d. Valle, *New Journal of Physics* **17**, 123021 (2015).
- ⁴⁸M. Davanço, C. S. Hellberg, S. Ates, A. Badolato, and K. Srinivasan, *Physical Review B* **89**, 161303(R) (2014).
- ⁴⁹J. P. Reithmaier, G. Şek, A. Löffler, C. Hofmann, S. Kuhn, S. Reitzenstein, L. V. Keldysh, V. D. Kulakovskii, T. L. Reinecke, and A. Forchel, *Nature* **432**, 197–200 (2004).
- ⁵⁰L. Monniello, C. Tonin, R. Hostein, A. Lemaitre, A. Martinez, V. Voliotis, and R. Grousson, *Physical Review Letters* **111**, 026403 (2013).